Crystal structure of κ-alumina: an X-ray powder diffraction, TEM and NMR study

Benoist Ollivier,[a]† Richard Retoux,[a] Philippe Lacorre,*[a] Dominique Massiot[b] and Gérard Férey[a]

[a]*Laboratoire des Fluorures, UPRES-A 6010, Université du Maine, Avenue Olivier-Messiaen, 72017 Le Mans Cedex, France*

[b]*Centre de Recherches sur la Physique des Hautes Températures, CNRS, 45071 Orléans Cedex 2, France*

The crystal structure of κ-alumina (κ-Al_2O_3) has been determined *ab initio* from an X-ray powder diffraction pattern (reliability factors: $R_{\mathrm{Bragg}}=0.046$, $R_p=0.090$, $R_{wp}=0.115$, $\chi^2=11.7$). The acentric structure (orthorhombic system, space group $Pna2_1$, $a=4.8437(2)$ Å, $b=8.3300(3)$ Å, $c=8.9547(4)$ Å, $Z=8$) is built up from a pseudo-close-packed stacking ABAC of oxygen atoms, with aluminium in octahedral and tetrahedral environments in a 3 : 1 ratio, which form zigzag ribbons of edge-sharing octahedra and corner-sharing tetrahedra. κ-Alumina was characterized using magic angle spinning (MAS) ^{27}Al NMR at two fields and multiple quantum magic angle spinning (3Q MQ MAS) ^{27}Al NMR. A high-resolution electron microscopy study confirmed the structure and showed the presence of two types of defects: antiphase boundaries and 120° disorientations. A model is proposed for these two types of defects, which leaves unchanged the pseudo-close-packed arrangement of the oxygen atoms and assumes a shift or 120° twinning of aluminium ions.

Many studies have already been devoted to alumina because of its importance to industrial applications and the richness of the structural forms of transition alumina. Three main and very complex dehydration paths exist to yield corundum (α-Al_2O_3) starting from aluminium trihydroxides. They depend on the starting material and the calcination conditions.[1–4] The two main aluminium trihydroxides are gibbsite (or hydrargillite) and bayerite (a third form exists, known as norstrandite, the structure of which is intermediate between those of gibbsite and bayerite). Calcination path 1 concerns the dehydration of gibbsite, through the formation of transition χ- and κ-Al_2O_3. It usually occurs for small grain sizes and slow heating rates. If the grains are larger and the heating rate is fast, local hydrothermal conditions occur such that aluminium oxyhydroxide (boehmite) is formed. Then dehydration occurs through path 2, which involves the formation of transition γ-, δ- and θ-Al_2O_3. Finally calcination of bayerite takes place through path 3, involving transition γ- and θ-Al_2O_3. The industrial process of the calcination of gibbsite mainly corresponds to path 1, with partial contribution of path 2.[5,6] Further modelling of this process requires a better knowledge of the structural arrangement of the involved intermediate phases, which should improve our understanding of the phase transformation mechanisms leading to corundum. However, up to now, very little was known about the crystal structure of the transition alumina formed during this process, mostly due to the poor crystallinity of these phases.

One of the many applications of alumina concerns its use as a coating for cemented carbide cutting tools. Such a coating is usually deposited by the chemical vapour deposition (CVD) technique. Under these conditions, the two most often encountered forms of deposited alumina are α- and κ-Al_2O_3. Several studies have been devoted to the characterization of such coatings and their mechanical properties (see for instance ref. 7–9). Their hardness is obviously linked to the atomic arrangement in both phases. The crystal structure of corundum α-Al_2O_3 has been very well known and referenced for a long time. Despite some claims,[7] no determination of the structural arrangement of κ-Al_2O_3 has, as yet, been undertaken. Up to now, to our knowledge, the most detailed structural work on κ-Al_2O_3 seems to be that of Liu and Skogsmo,[10] who carried out a convergent-beam electron diffraction (CBED) study on a sample obtained by CVD. It allowed them to determine the space group and to propose a hypothesis for a structural model.

In this article, we present a detailed study of the crystal structure of κ-Al_2O_3, using X-ray diffraction, magic angle spinning (MAS) and multiple quantum magic angle spinning (MQ MAS) ^{27}Al nuclear magnetic resonance spectroscopy and transmission electron microscopy (preliminary account of this study given in ref. 11).

Experimental

Synthesis

The main obstacle in the structural characterization of transition aluminas is their often poor degree of crystallinity, which sometimes results in partial occupation of crystallographic sites. An additional problem concerning κ-Al_2O_3 is the difficulty to obtain it in significant amounts as a pure phase. Several attempts were made to improve the crystalline quality and purity of κ-Al_2O_3. Some involved the addition of mineralizers while others focused on the annealing process.

The starting material, the precursor of the sample used for the structural determination, was an industrial sample of aluminium trihydroxide with low sodium content (gibbsite) prepared through the Bayer process and provided by Aluminium Pechiney Gardanne (sample SH950). The impurity contents of this hydroxide were determined to be about 10 ppm Si, 15 ppm Fe, 15 ppm Cu and 450 ppm Na_2O, and its granulometry to be $d_{50}=79$ µm.

Different annealing processes were applied in order to obtain good quality κ-Al_2O_3 samples. The best crystallinity of the κ phase was obtained for a preheating at 600 °C for 1 h, followed by a 6 day annealing at 875 °C, both performed in a pinched platinum tube in air. The X-ray diffraction pattern of the corresponding sample [see Fig. 1(*b*)] showed the presence, in addition to the majority phase of κ-Al_2O_3 (JCPDS file no. 040878), of some amounts of poorly crystallized θ-Al_2O_3 (JCPDS file no. 350121) and of a few percent of δ-Al_2O_3 (JCPDS file no. 160394) and well crystallized α-Al_2O_3 (JCPDS file no. 431484). Further annealing at the same temperature leads to the crystallization of α- at the expense of κ-Al_2O_3, so that a 6 day annealing at 875 °C appeared to be a good

---

† Present address: Génie et Elaboration des Matériaux, Pechiney Centre de Recherches de Voreppe, Centr'Alp B.P. 27, 38340 Voreppe, France.

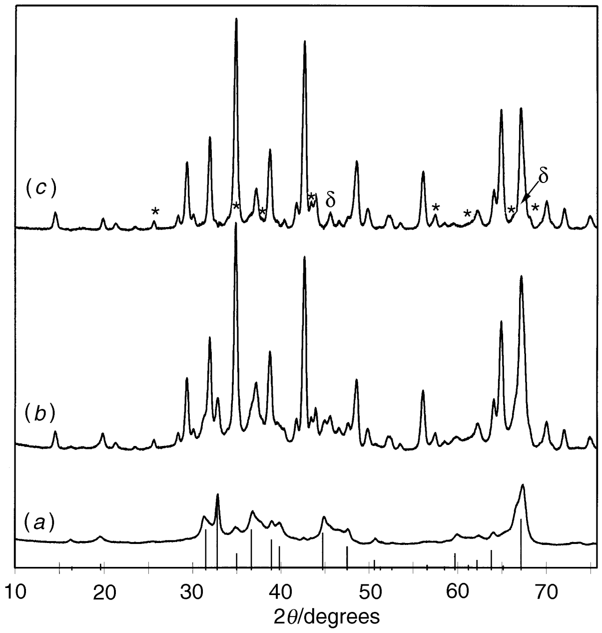

Fig. 1 X-Ray diffraction patterns (Cu-Kα) of poorly crystallized θ-Al_2O_3 (*a*) and of the sample containing κ-Al_2O_3 as a majority phase (*b*). The structural refinement was performed on the difference pattern (*c*) obtained by subtracting (*a*) from (*b*) (see text). The vertical lines correspond to the peak positions and intensities of θ-Al_2O_3 according to the JCPDS file no. 350121. The stars indicate the α-Al_2O_3 impurity lines, and the δ signs indicate the two most intense reflections of impurity δ-Al_2O_3, with almost equal intensity.

compromise between crystallinity and impurity content. To avoid problems due to the poorly crystallized θ-Al_2O_3 impurity during the structural refinement, a diffraction pattern of pure θ-Al_2O_3 was recorded in order to subtract it from the κ-Al_2O_3 pattern. The θ-Al_2O_3 sample was obtained by annealing the trihydroxide precursor first for 1 h at 600 °C, then for 5 min at 1100 °C.

For the NMR spectroscopy study, a technique which is less sensitive to long-range order, we focused on purity rather than on crystallinity and used another, less crystallized but purer sample, free of any α-Al_2O_3 phase and with only about 5% θ-Al_2O_3. This sample was obtained by dehydration of another industrial sample of gibbsite (sample SH500 provided by Aluminium Pechiney Gardanne, containing 3550 ppm Na_2O), first preheated for 1 h at 300 °C, then heated from room temperature up to 1150 °C with a heating rate of 5 °C min^{-1}, and finally cooled to room temperature.

X-Ray diffraction

The X-ray diffraction pattern was recorded on a Siemens D500 diffractometer with the following conditions: 2θ range = 10–140 °, step = 0.020 °, slit = 0.15, counting rate = 35 s per step. The diffraction pattern of the pure θ-phase sample [Fig. 1(*a*)] was recorded using the same conditions, then subtracted from the κ pattern [Fig. 1(*b*)] with an appropriate coefficient. Structural refinements were done on the corrected pattern [Fig. 1(*c*)], using programs FULLPROF,[12] SHELXS-86[13] and SHELXL-93.[14] The final refinement with FULLPROF was done using 5876 points in a 2θ range of 12.5–130 °, which includes 327 reflections for the κ phase.

NMR spectroscopy

High-resolution ^{27}Al magic angle spinning (MAS) and multiple-quantum magic angle spinning (3Q MQ MAS) NMR experiments[15–20] have been carried out on powdered samples of κ-Al_2O_3 at two different principal fields: 7 T (ν_0 = 78.21 MHz) for 15 kHz MAS and MQ MAS and 11.7 T (ν_0 = 130.32 MHz) for 12.5 kHz MAS. All experiments have been recorded using Bruker solid-state spectrometers (MSL 300 and ASX 500) with standard double bearing magic angle spinning probeheads free of background signals. The MAS spectra have been acquired using small pulse angles (*ca.* $\pi/12$) to ensure a homogeneous irradiation of the different lines, with a recycle delay of 1 s. The 3Q MQ MAS spectrum has been acquired (while spinning at magic angle) with a two pulse excitation sequence and the data further processed according to the previously described Echo/Antiecho protocol 6, using the RMN program.[21] Spectrum modelling has been done using a modified version of Bruker Winfit program.[22]

Electron microscopy

The HREM and ED studies were performed on a 200 kV JEOL 2010 electron microscope (tilt ±30 °). The specimens for electron microscopy were prepared by suspending very thin crystals in *n*-butanol (obtained from a thorough grinding of a powdered sample; few droplets of the suspension were put on a carbon coated holey film). The series of programs written by Stadelman[23] was used to simulate high-resolution images at different focus using the multislice method (with spherical aberration constant $C_s = 1$, spread of focus $\Delta_F = 10$ Å).

Structure determination and description

Structural determination

The determination of the cell parameters was achieved using the program TREOR[24] with the 22 first observed reflections. The best and most probable solution (figure of merit M_{20} = 19, F_{20} = 15) was obtained for an orthorhombic cell with parameters close to those given in ref. 10. The observed reflections agree well with the space group $Pna2_1$ determined by Liu and Skogsmo from their CBED study. However, the simulated X-ray diffraction pattern of the structural model‡ proposed by Liu and Skogsmo [Fig. 10(*b*) of ref. 10] proved to be totally different from the observed X-ray pattern of κ-Al_2O_3. The structural determination was carried out using the acentric space group $Pna2_1$. The observed structure factors were extracted using the program FULLPROF in the 'Profile Matching' mode. The option TREF20 of direct methods (program SHELXS86) allowed us to determine the positions of some of the atoms. The discrimination between aluminium and oxygen was based on interatomic distances. The other atoms were located by Fourier difference syntheses (program SHELXL-93). The final refinement was performed using the Rietveld procedure of the program FULLPROF. During this process, the impurity phases α- and δ-Al_2O_3 were treated in the Rietveld-refinement mode and Profile Matching mode, respectively (for δ-Al_2O_3, the reflections used were those of the JCPDS file no. 160394). The refinement of atomic occupation factors in κ-Al_2O_3, originally fixed to unity, did not lead to any improvement of the reliability. During the final step, a total of 63 parameters were refined, including 6 background parameters and 45 parameters related to the κ-Al_2O_3 phase. Among these, 29 atomic position parameters and 5 temperature

---

‡ In ref. 10, a mistake in the text makes the structural description inconsistent with both space group $Pna2_1$ and Fig. 10(*b*). The structural model of κ-Al_2O_3 is presented on p.430 as the stacking along *c* of successive layers of Al in octahedral and tetrahedral coordination (called α and β', respectively), according to the sequence $\alpha\alpha\beta'\beta'\alpha$: such a sequence is inconsistent with the presence of a 2_1 axis along *c*, which imposes that every other plane along *c* is of the same type, and thus cannot contain aluminium atoms with different coordination. The mistake comes from the wrong assertion that β' sites have tetrahedral coordination, which is obviously not the case in Fig. 10(*b*). We based our X-ray diffraction calculation of the structural model of ref. 10 on the idealized arrangement shown in Fig. 10(*b*), which can be described using space group $Pna2_1$.

factors were refined, the temperature factors of all oxygen atoms being constrained to the same value. The peak profile was fixed to pseudo-Voigt type, with η parameter refined to about 0.60. Low-angle asymmetry of peak shape was taken into account, as well as preferred orientation (almost negligible). The final reliability factors are $R_{\mathrm{Bragg}}=0.046$, $R_{\mathrm{F}}=0.033$, $R_{\mathrm{p}}=0.090$, $R_{\mathrm{wp}}=0.115$ ($\chi^2=11.7$). The observed and calculated patterns are shown in Fig. 2 and Table 1 lists atomic parameters.

Description of the structure

The crystal structure of κ-Al_2O_3 does not correspond to the model presented in ref. 10. Its representation in terms of coordination polyhedra is shown in Fig. 3 and 4 and can be described as an ABAC pseudo-close-packed stacking of oxygen atoms, with aluminium occupying octahedral and tetrahedral sites. This type of stacking of layers is also observed in tohdite $5Al_2O_3\cdot H_2O$,[25] whose dehydration leads first to κ′-Al_2O_3[26] with the same ABAC oxygen atoms stacking, then to κ-Al_2O_3. It should be noted that the oxygen stackings of the transition alumina originating from another dehydration path of gibbsite (namely γ-Al_2O_3, δ-Al_2O_3 and θ-Al_2O_3) are always of the type ABCABC.

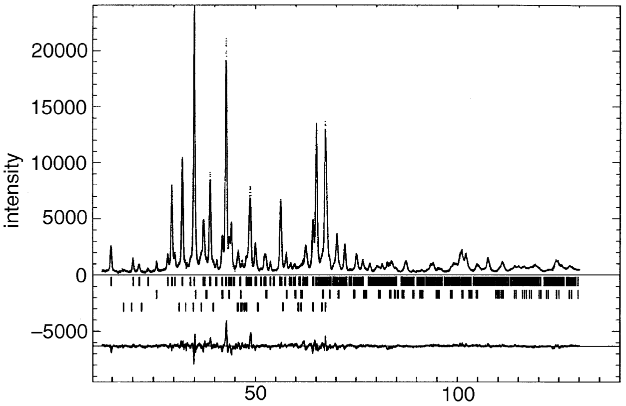

Fig. 2 Observed (dots) and calculated (line) diffraction diagrams after the κ-phase structure refinement with the program FULLPROF.[12] The difference pattern (obs.−calc.) is shown at the bottom, as well as the peak positions for the κ-phase (upper), and α- (middle) and δ- (lower) impurity phases.

Table 1 Atomic parameters for κ-Al_2O_3[a]

atom	site	x	y	z	B/Å^2
Al(1)	4a	0.6787(6)	0.8416(4)	0	0.41(1)
Al(2)	4a	0.1846(11)	0.3432(7)	0.7868(7)	1.32(9)
Al(3)	4a	0.8115(8)	0.6489(5)	0.6972(7)	0.16(6)
Al(4)	4a	0.6677(7)	0.4696(3)	0.9993(11)	0.35(5)
O(1)	4a	0.3290(16)	0.8313(9)	0.8927(7)	0.27(4)
O(2)	4a	0.0248(12)	0.4908(7)	0.6292(12)	0.27(4)
O(3)	4a	0.4717(13)	0.6647(8)	0.6381(11)	0.27(4)
O(4)	4a	0.5145(15)	0.6728(7)	0.1212(9)	0.27(4)
O(5)	4a	0.8608(16)	0.3301(11)	0.8662(7)	0.27(4)
O(6)	4a	0.3360(17)	0.4992(7)	0.9000(8)	0.27(4)

[a] Space group $Pna2_1$, $Z=8$, $a=4.8437(2)$ Å, $b=8.3300(3)$ Å, $c=8.9547(4)$ Å.

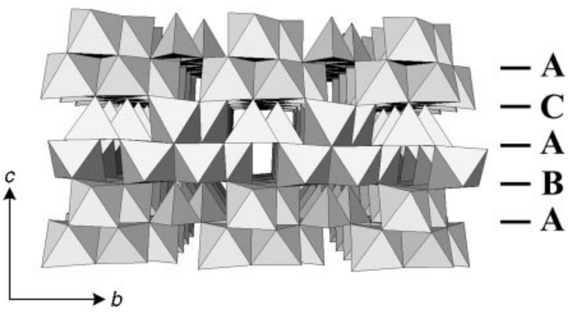

Fig. 3 Elevation view of the κ-Al_2O_3 crystal structure showing the ABAC pseudo-close-packed stacking of oxygen atoms

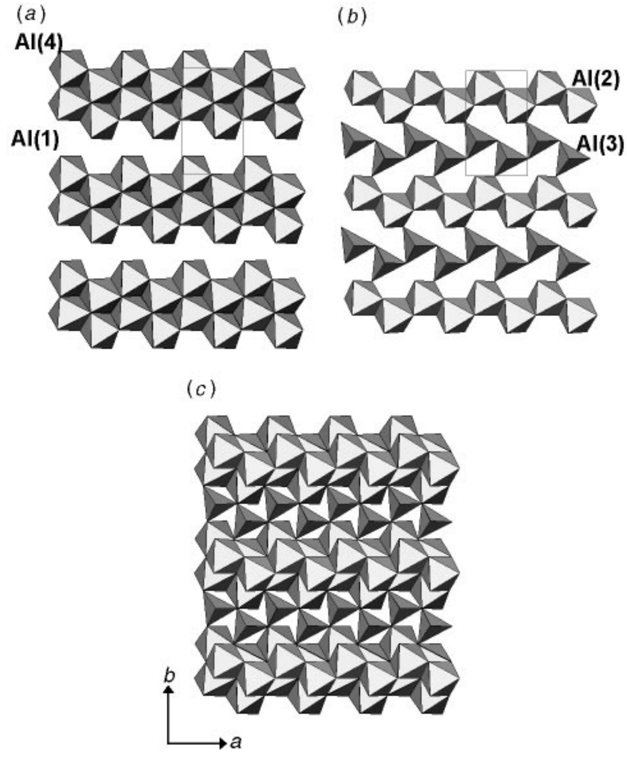

Fig. 4 The two types of polyhedral layers [BA] (*a*) and [AC] (*b*) present in κ-Al_2O_3, as well as their mode of stacking (*c*)

The position of Al^{3+} cations in between oxygen planes defines two types of polyhedral layers, shown in projection along the *c* axis in Fig. 4. Layer [BA] is built up from double zigzag ribbons of [AlO_6] edge-sharing octahedra, these double ribbons being isolated from each other within the layer [Fig. 4(*a*)]. Layer [AC] is formed from alternating single ribbons of octahedra [AlO_6] joined by edges and single ribbons of corner-sharing tetrahedra [AlO_4] [Fig. 4(*b*)]. Connections between ribbons occur through polyhedra vertices. Two successive layers [Fig. 4(*c*)] share polyhedra edges and vertices. Each tetrahedron shares two of its vertices with another tetrahedron and an octahedron. The other two vertices are shared with three octahedra. Within [AC] layers, all the tetrahedra point toward the same directions: this characteristic shows the intrinsic acentricity of the structure. One unit cell is built up from the stacking of four different layers, alternatively of the [BA] and [AC] types.

Distances, angles and valences[27] of Al—O bonds in each polyhedron are displayed in Tables 2 and 3. Polyhedra are more or less distorted, the less being octahedron [$Al(1)O_6$], with Al—O distances between 1.72 and 1.96 Å. In comparison, distances (and bond valences) in the [$Al(2)O_6$] polyhedron are more heterogeneous: bond Al(2)—O(4) is much weaker than the other Al—O bonds ($d=2.27$ Å), leading to a coordination of the type V+I rather than VI for this aluminium site. Al(2) has the largest thermal factor (see Table 1) in agreement with this strong distortion. The NMR spectroscopy study presented in the following section confirms the presence of a very distorted neighbourhood for one aluminium site in the structure. The aluminium coordination octahedra can be classified according to their increasing distortion: Al(1) < Al(4) < Al(2).

Table 2 Interatomic distances and angles in κ-Al_2O_3

Al(1)	O(6)	O(1)	O(4)	O(1)	O(4)	O(2)
O(6)	**1.772(6)**	98.6(6)	176.4(3)	99.1(6)	88.2(7)	92.3(7)
O(1)	2.768(9)	**1.878(7)**	83.6(7)	92.9(7)	85.1(7)	169.0(3)
O(4)	3.717(5)	2.551(9)	**1.946(6)**	83.6(7)	89.2(6)	85.6(6)
O(1)	2.834(10)	2.775(10)	2.595(10)	**1.949(7)**	172.7(6)	83.2(7)
O(4)	2.600(9)	2.595(10)	2.742(9)	3.900(10)	**1.959(7)**	97.4(6)
O(2)	2.696(11)	3.823(4)	2.657(7)	2.598(12)	2.947(8)	**1.963(7)**
Al(2)	O(5)	O(6)	O(5)	O(2)	O(4)	O(4)
O(5)	**1.725(9)**	100.6(8)	102.4(8)	88.8(8)	157.7(8)	81.0(8)
O(6)	2.715(10)	**1.804(7)**	99.2(7)	96.3(7)	99.3(7)	172.4(3)
O(5)	2.765(10)	2.762(9)	**1.822(10)**	158.8(4)	84.2(8)	87.6(7)
O(2)	2.633(11)	2.857(12)	3.782(4)	**2.026(11)**	79.0(8)	76.2(8)
O(4)	3.738(11)	2.968(8)	2.626(10)	2.616(8)	**2.084(9)**	78.0(7)
O(4)	2.626(11)	4.063(4)	2.850(9)	2.657(8)	2.742(9)	**2.268(7)**
Al(3)	O(3)	O(1)	O(2)	O(3)		
O(3)	**1.734(7)**	110.0(7)	120.2(6)	104.6(6)		
O(1)	2.862(10)	**1.760(8)**	112.4(6)	100.9(7)		
O(2)	3.046(8)	2.944(8)	**1.781(8)**	106.5(6)		
O(3)	2.808(9)	2.757(9)	2.882(9)	**1.815(6)**		
Al(4)	O(3)	O(6)	O(5)	O(2)	O(1)	O(4)
O(3)	**1.804(13)**	95.1(8)	103.6(7)	88.8(8)	163.3(3)	90.5(7)
O(6)	2.698(10)	**1.853(9)**	101.9(7)	160.3(7)	90.0(8)	80.8(8)
O(5)	2.920(10)	2.922(10)	**1.910(7)**	95.9(8)	90.9(8)	165.2(3)
O(2)	2.606(8)	3.715(11)	2.842(10)	**1.918(9)**	81.3(9)	79.9(8)
O(1)	3.829(4)	2.775(10)	2.835(11)	2.598(12)	**2.067(11)**	74.5(8)
O(4)	2.816(8)	2.600(10)	4.022(4)	2.616(8)	2.551(9)	**2.146(5)**

Table 3 Cation valences[a] in κ-Al_2O_3

Al(1) 3.02	Al(2) 2.97	Al(3) 2.89	Al(4) 2.81
O(6) 0.72	O(5) 0.82	O(3) 0.80	O(3) 0.66
O(1) 0.54	O(6) 0.66	O(1) 0.74	O(6) 0.58
O(4) 0.45	O(5) 0.63	O(2) 0.70	O(5) 0.50
O(1) 0.45	O(2) 0.36	O(3) 0.64	O(2) 0.49
O(4) 0.43	O(4) 0.31		O(1) 0.33
O(2) 0.43	O(4) 0.19		O(4) 0.26

[a] Calculated according to formula $v_{ij}=\exp[(R_{ij}-d_{ij})/b]$ with parameters $b=0.37$ Å and $R_{ij}=1.651$ Å (from ref. 27).

NMR spectroscopy study

Fig. 5 presents the ^{27}Al MAS and MQ MAS spectra of κ-Al_2O_3. Concerning the MAS spectra [Fig. 5(*a*)], as expected, the high-field spectrum (11.7 T) is better resolved because the second-order quadrupolar interaction broadening is proportional to the inverse of the squared Larmor frequency (or principal field). At both fields the tetrahedral contribution (Al_{IV}) is clearly visible with a well defined second-order quadrupolar shape, the quadrupolar frequency can be estimated to be close to *ca.* 800 kHz. The octahedral contribution (Al_{VI}) shows smooth discontinuities visible only at low field (7 T) with a supplemental contribution appearing at the right side in the high field spectrum [indicated by an arrow on Fig. 5(*a*)]. From these observations, we can conclude that the Al_{VI} region consists of overlapping lines having intermediate quadrupolar couplings (main Al_{VI} line) plus a supplemental contribution having high quadrupolar couplings, the latter being only visible at the higher field. This highly deformed line cannot be further analysed but is easily ascribed to the most asymmetric site of the κ-Al_2O_3 structure: Al_{V+I} [Al(2) site]. Its quadrupolar coupling is estimated to be >1.5 MHz.

The ^{27}Al 3Q MQ MAS experiment [Fig. 5(*b*)] yields a way of obtaining a better resolution of these different contributions. The two dimensional MQ MAS spectrum correlates an isotropic dimension (F_1 vertical axis) to the usual MAS dimension (F_2), slightly modified by the triple quantum excitation. In the

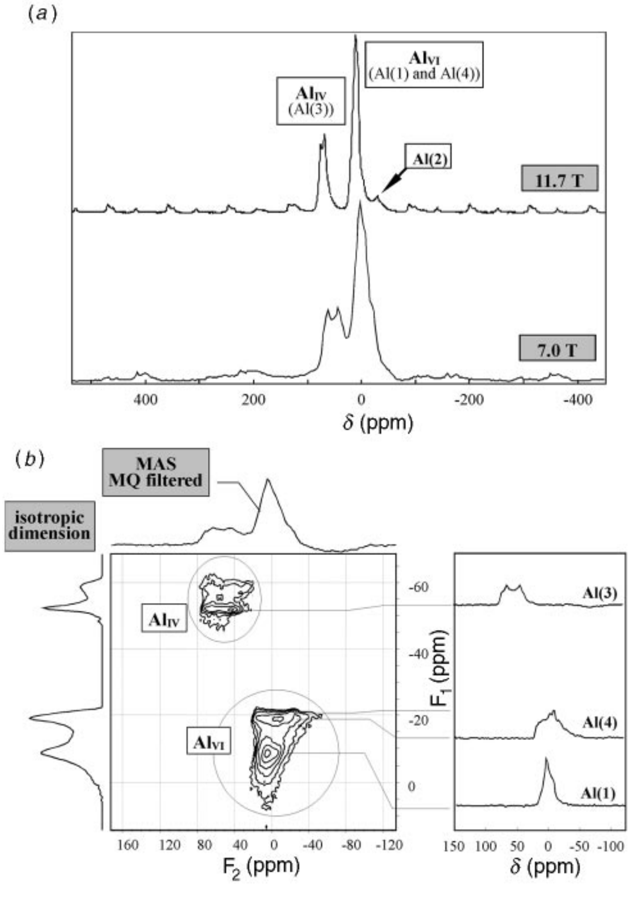

Fig. 5 ^{27}Al NMR spectra of κ-Al_2O_3: (*a*) MAS spectra at 7.0 and 11.7 T; (*b*) 3Q MQ MAS spectra at 7.0 T. The very distorted site Al(2) is only visible at the higher field in MAS while the Al(1), Al(3) and Al(4) sites are fully resolved in the MQ MAS spectrum.

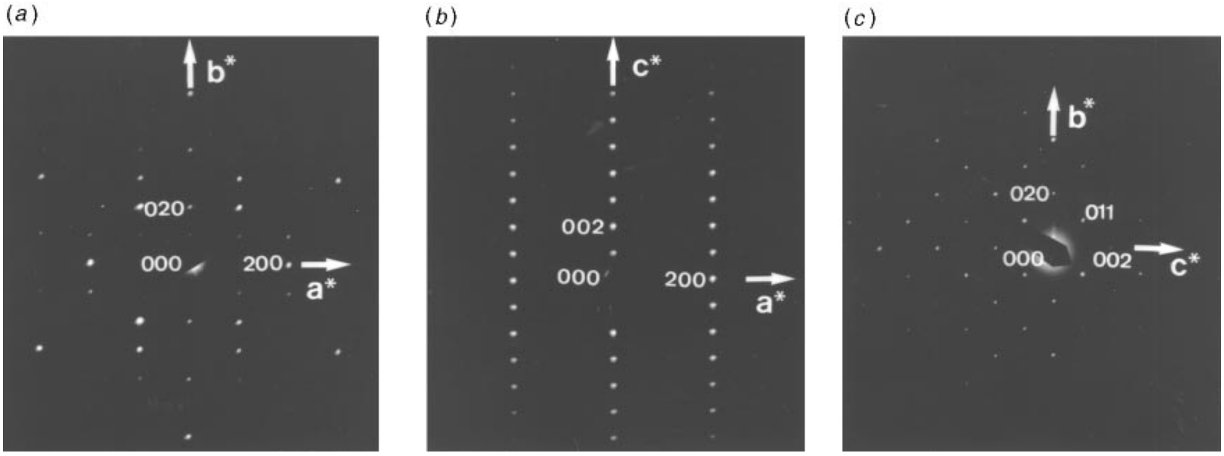

Fig. 6 Electron diffraction patterns of κ-Al_2O_3 along the three cell axes: (*a*) [001]*, (*b*) [010]*, (*c*) [100]*

isotropic dimension the second-order quadrupolar broadening is removed and the resolution enhanced. In such an experiment, an ideal site, described by its chemical shift position and its quadrupolar interaction, would give a sharp horizontal line, with its MAS triple quantum filtered spectrum in the cross section. This is typically what we observe for the main feature of the Al_{IV} region whose cross section can be directly modelled (Table 4). This feature is unambiguously ascribed to the Al_{IV} site of the κ-Al_2O_3 structure [site Al(3)]. The complex Al_{VI} line of the MAS spectrum splits in two parts. The first part appears as a close to horizontal ridge in the two dimensional spectrum but its shape is not perfectly characteristic of a unique quadrupolar tensor. This may be due to the imperfect triple/single quantum transfer and/or to slightly dispersed quadrupolar coupling and asymmetry parameters. In any case, we can measure its chemical shift position and estimate its quadrupolar tensor which are reported in Table 4. The second part of the Al_{VI} region is nearly featureless and widens in the isotropic dimension. It gives rise to an ovoid shape in the two dimensional plot. The only possible interpretation of this feature is an average site with dispersed quadrupolar interaction parameters. Nevertheless, the quadrupolar parameter is less for this site than for the previously described other Al_{VI} contribution. Based on this observation and considering that the quadrupolar interaction (and thus the electric field gradient) is an image of the asymmetry of the site, we ascribe the former contribution to the Al(4) site (Al—O distances ranging from 1.804 to 2.146 Å) and the latter to the Al(1) (Al—O distances ranging from 1.722 to 1.963 Å) site.

Transmission electron microscopy study

Electron diffraction

Most of the platelet like crystals observed by electron microscopy were oriented along [001], other orientations being very difficult to observe. However, reconstitutions of the reciprocal lattice were performed, and the extinction conditions are compatible with space group $Pna2_1$ (see Fig. 6). The conditions of systematic reflection are $0kl$, $k+l=2n$ [Fig. 6(*c*)], $h0l$, $h=2n$; $h00$, $h=2n$ [Fig. 6(*a*),(*b*)]; $0k0$, $k=2n$ [Fig. 6(*a*)] and $00l$, $l=2n$ [Fig. 6(*c*)]. In Fig. 6(*b*), $00l$ reflections with $l=2n+1$ arise from double diffraction phenomena. Along the c* direction, diffuse streaks are sometimes observed. This phenomenon suggests the presence of defects along the c direction. We tried to image these defects at high-resolution, but no significant contrast could be interpreted on the [100] or [010] observations.

Very frequent defects were observed along the zone axis [001], resulting in the presence of additional spots arranged in a pseudo-hexagonal pattern [see Fig. 7(*a*)]. As proposed by Liu and Skogsmo in their convergent beam study,[10] these patterns can be interpreted as the superimposition of three different lattices disoriented by 120° from each other. High-resolution images confirm this point [Fig. 7(*b*)]. Here, the contrasts observed on the three domains of the crystal are slightly different due to very small disorientations of the [001] zone axis. While the Fourier transform of the whole image [Fig. 7(*c*)] is comparable to the pseudo-hexagonal pattern of Fig. 7(*a*), the high-resolution image of each individual crystal has a Fourier transform [Fig. 7(*b*)] equivalent to the diffraction pattern of Fig. 6(*a*). We will see below that these defects can be interpreted as 120° twinnings of the κ-Al_2O_3 structure.

High resolution

In order to confirm the validity of the structure determined by X-ray powder diffraction, we have compared high-resolution images along the c axis obtained at different focus values to

Table 4 NMR parameters of the different sites observed by ^{27}Al NMR spectroscopy for κ-Al_2O_3

site	CN^b	δ	C_Q/MHz	η_Q	δ_{F_1}/ppm
Al(1)	VI	*ca.* 13	500	—	−9
Al(2)	V+I	—^{c}	>1.5	—	—
Al(3)	IV	81.5	760	0.3	−52
Al(4)	VI	18	850	—	−20

^{a} δ = chemical shift; C_Q = quadrupolar coupling constant; η_Q = quadrupolar asymmetry parameter; δ_{F_1} = position in the isotropic dimension. ^{b}CN = coordination number. ^{c}Not determined.

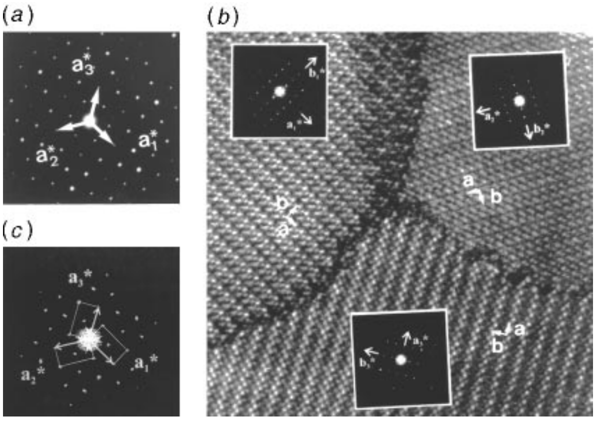

Fig. 7 120° twinnings in a crystal of κ-Al_2O_3: (*a*) SAED pattern of the whole crystal; (*b*) HREM image showing the three disoriented domains; inserts show the Fourier transforms of each individual domain; (*c*) Fourier transform of the whole high resolution image [compare with (*a*) and with the superimposition of the three Fourier transforms of (*b*)]

images simulated from the structural model (Fig. 8). Due to the compact stacking of oxygen atoms, the right contrasts are very difficult to observe. A very small disorientation of the crystal induces important modifications of the contrasts, in particular on the intensity of white dots which should be equivalent. This is particularly true on thick parts of the crystals [as for example in Fig. 11(*b*)]. The best contrasts are obtained on thin parts of the crystals, close to the edges. Fig. 8 shows a comparison between observed and simulated images at different focus values: the agreement is fairly good. Two main contrasts can be interpreted. For a defocus close to -300 and -500 Å, white sticks (-300) or dots (-500) are representative of the aluminium atoms of the [BA] layers in octahedral environments, while the aluminium atoms of the [AC] layers appear in black. For a defocus close to -850, -950 Å, white dots are representative of the aluminium atoms in octahedral and tetrahedral environments forming [AC] layers.

As already mentioned, the most often observed orientation was [001]. As can be seen in Fig. 9, very numerous defects were observed along this direction, belonging to two categories: antiphase boundaries (A) and disoriented domains (B,C).

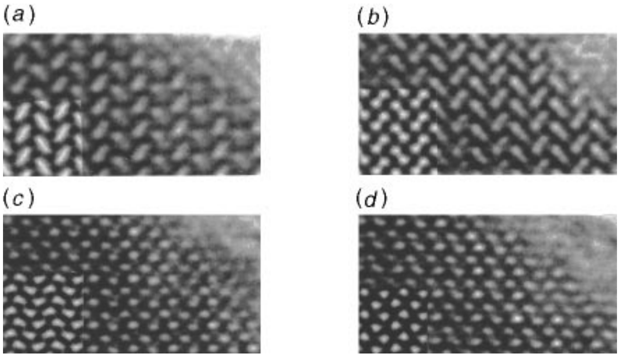

Fig. 8 Comparison between [001] observed and calculated (inserts) through focus series images of κ-Al_2O_3. Focus values are in Å and the most evident contrasts are obtained for defocus values close to -400 Å and -900 Å (see text). Calculated images in the inserts correspond to a crystal thickness of 27 Å, with defocus values of (*a*) -300 Å, (*b*) -500 Å, (*c*) -850 Å, (*d*) -950 Å.

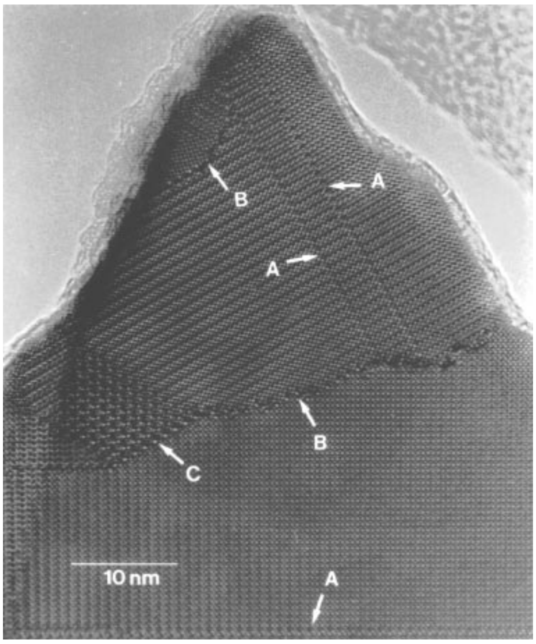

Fig. 9 High-resolution image along the *c* axis showing two types of defects observed in κ-Al_2O_3: antiphase boundaries (A); disoriented domains (B and C)

We will now give a description of the two defect families in relationship to the crystal structure.

Antiphase boundaries

Defects of this type are shown in Fig. 9 (indicated by A) and Fig. 10(*a*). They most often develop along the *b* axis of the structure. A shift of the structural pattern can clearly be seen across the defects. Fig. 10(*b*) and (*c*) present a model which can explain the atomic location around the boundary, within [BA] and [AC] layers, respectively. In the high-resolution image, white spots are representative of aluminium atoms belonging to the [AC] layer [*cf.* white dots in Fig. 10(*c*)]. The presence of such defects is made possible by the pseudo-close-packed stacking of the oxygen atoms, and by the zigzag structure of the ribbons. In such a model, the shift across the domain boundary corresponds to the displacement of aluminium atoms of half the O—O distance along the *b* axis, that is about 1.35 Å, in good agreement with the observed value. The oxygen stacking thus remains unchanged across the defect.

Such antiphase boundaries can occur as isolated defects, but multi-defect zones can also be found, with several successive atomic shifts. Fig. 11(*a*) shows a multi-defect boundary formed by three successive atomic displacements, resulting in a total shift of *ca.* 4 Å (alignment of 5 Al atoms within the boundary). In Fig. 11(*b*), two elementary antiphase boundaries combine to form a double defect boundary involving two successive atomic shifts, leading to a total shift of *ca.* 2.7 Å.

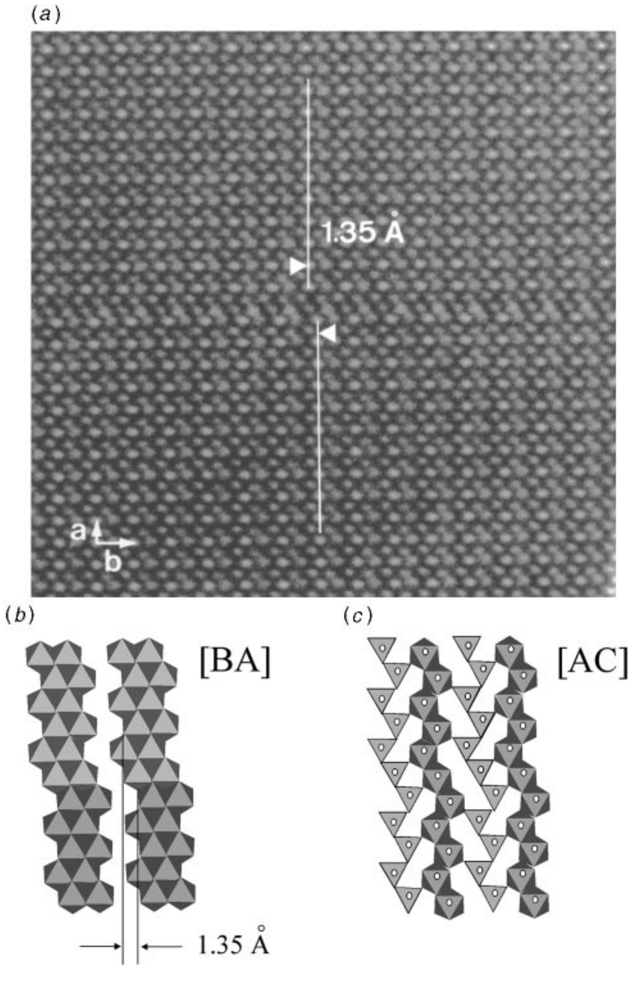

Fig. 10 Single antiphase boundary in κ-Al_2O_3: (*a*) high-resolution image showing an atomic shift of about 1.35 Å across the boundary (one atomic shift, resulting in three aligned Al atoms across the boundary); model representations of this defect within the [BA] (*b*) and [AC] (*c*) layers

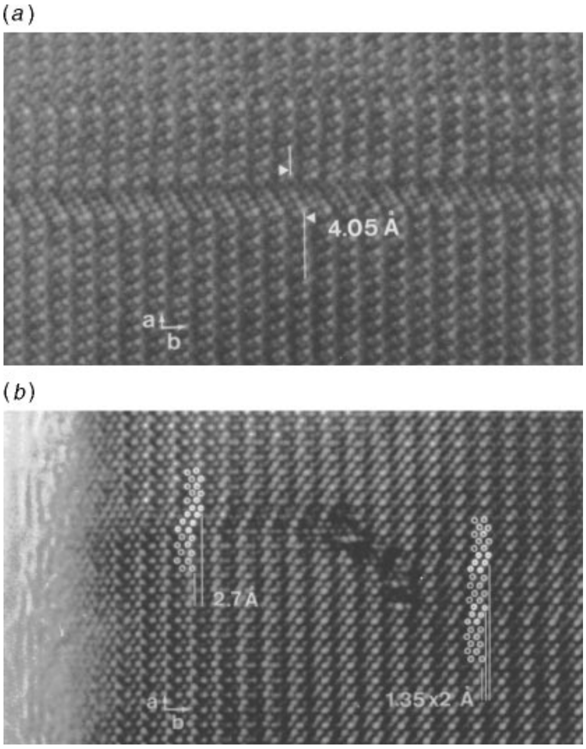

Fig. 11 Multiple antiphase boundaries in κ-Al_2O_3: (*a*) three successive atomic displacements resulting in a total shift of 4.05 Å (5 Al atoms aligned within the boundary); (*b*) two isolated antiphase boundaries [*cf.* Fig. 10(*a*)] combine to give a double-defect boundary (four Al atoms aligned within the boundary)

Disoriented domains

The second kind of defect [Fig. 9(B and C) and Fig. 12(*a*)] can also be very well explained if one considers a twinning mechanism involving aluminium atoms only, the oxygen stacking remaining intact. Fig. 12(*b*) proposes a model for such a twinning, permitted by the pseudo-close-packed arrangement of the oxygen atoms. It results in two domains disoriented by 120 ° from each other.

It may happen that the boundary between two such disoriented domains is more or less well defined. Fig. 13(*a*) shows a wide perturbed region between two disoriented crystals, forming a Moiré pattern. In such a case, it is very unlikely that the two crystals have just developed side by side; they most probably overlap along the *c* direction. Fig. 13(*b*) and (*c*) give a schematic representation of both types of twinning.

Finally, it can be noted that besides quite large domains free of defects, small parts of crystals may present numerous defects involving very disturbed contrasts (see Fig. 14). Such poorly organized parts can be seen as the remains of poorly crystallized transition alumina.

Summary and conclusion

We have been able to synthesize by a six day annealing at intermediate temperature a pure enough and well crystallized form of κ-Al_2O_3, suitable for structural determination. The crystal structure of κ-Al_2O_3 has been determined *ab initio* from an X-ray powder diffraction pattern. It consists of the stacking of pseudo-close-packed layers of oxygen atoms (ABAC type) in between which aluminium atoms are inserted in octahedral and tetrahedral coordination (in the ratio 3:1). NMR spectroscopy and electron microscopy studies were carried out and their results were found to be consistent with the structural study. In addition, the electron microscopy study allowed us to propose models for two frequent defects observed in the structure. Apart from these defects, an interesting feature of

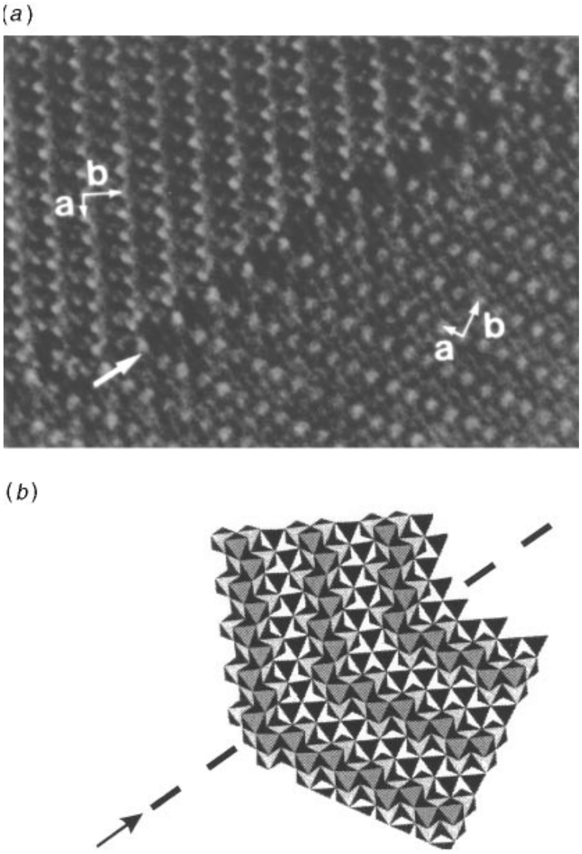

Fig. 12 Twinning boundary observed in κ-Al_2O_3 (*a*) and its model representation (*b*)

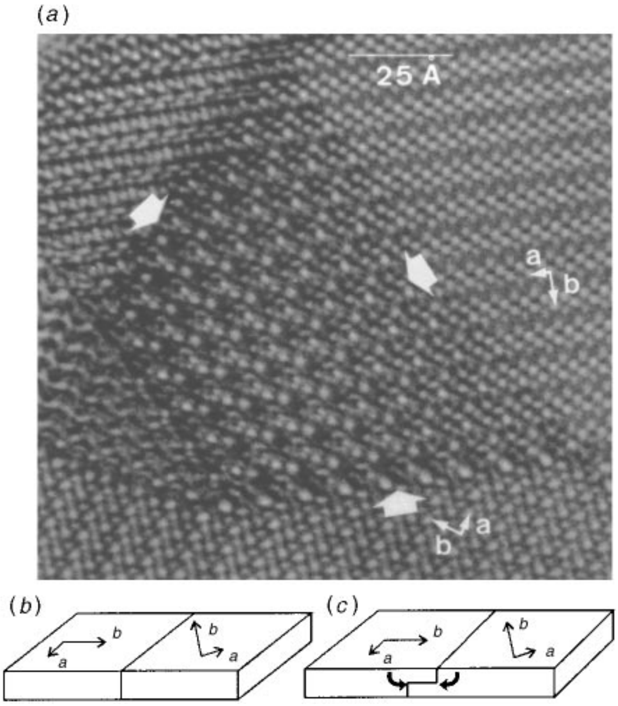

Fig. 13 (*a*) High-resolution image showing the overlap of two disoriented domains; (*b*) schematic representation of a regular twinning, with straight boundary as in Fig. 9(B) and 12; (*c*) schematic representation of an irregular twinning with overlapping domains, as in Fig. 9(C) and 13(*a*)

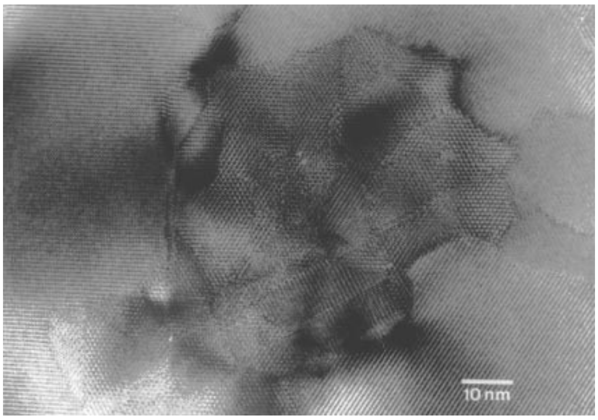

Fig. 14 Image showing very disturbed contrasts resulting from the accumulation of numerous defects in a small part of a crystal

the structure of κ-Al_2O_3 is the good ordering of both anions and cations, which is not the case for most of the transition aluminas, such as κ′, η, γ or δ, where some aluminium sites are not fully occupied. The coexistence of aluminium in tetrahedral and octahedral coordination as observed in κ-Al_2O_3 seems to be a common feature to several transition aluminas (*e.g.* η, γ, δ or θ). A distinctive point of the structure of κ is the presence of a very distorted octahedral environment for one of the atoms (V+I neighbours), which is responsible for a very broad NMR signal.

It is expected that the knowledge of the structure of κ-Al_2O_3 will trigger more work on the phase transformation processes leading to corundum α-Al_2O_3 and on the structure–property relationships in κ-Al_2O_3 coatings.

The authors are deeply grateful to Pechiney company for financial support of this study. They also express special thanks to Professor M. Hervieu (laboratoire CRISMAT, Caen, France) for a critical reading of the manuscript.

References

1 K. Wefers and C. Misra, Alcoa Technical Paper no. 19, revised, Alcoa Laboratories, Pittsburg, PA, USA, 1987.

2 J. H. DeBoer, J. M. H. Fortuin and J. J. Steggerda, *Proc. Kon. Ned. Akad. Wetensch.*, 1954, **57**, 434.

3 O. Glemser and G. Rieck, *Angew. Chem.*, 1956, **68**, 182.

4 J. Rouquerol, F. Rouquerol and M. Ganteaume, *J. Catal.*, 1975, **36**, 99.

5 H. C. Stumpf, A. S. Russel, J. W. Newsome and C. M. Tucker, *Ind. Eng. Chem.*, 1950, **42**, 1398.

6 R. Tertian and D. Papée, *J. Chim. Phys.*, 1958, **55**, 341.

7 J. Echigoya, T. Hyakubu, Z. T. Liu, K. Sasaki and H. Suto, *Surf. Coat. Technol.*, 1994, **67**, 111.

8 H. G. Prengel, W. Heinrich, G. Roder and K. H. Wendt, *Surf. Coat. Technol.*, 1994, **68/69**, 217.

9 M. Halvarsson, H. Nordén and S. Vuorinen, *Surf. Coat. Technol.*, 1994, **68/69**, 266.

10 P. Liu and P. Skogsmo, *Acta Crystallogr., Sect. B*, 1991, **47**, 425.

11 R. Retoux, B. Ollivier, P. Lacorre and G. Ferey, *Proceedings of the XIth European Congress on Microscopy, EUREM'96*, Dublin, Ireland, 26–30 Aug. 1996, M4–10. B. Ollivier, R. Retoux, D. Massiot, P. Lacorre, and G. Ferey, *Résumés des Journées de la Division Chimie du Solide*, Paris, France, 4–6 Sept. 1996, B28.

12 J. Rodriguez-Carvajal, *Abstracts of the Satellite Meeting on Powder Diffraction of the XV Congress of the IUCr*, Toulouse, France, 1990, 127.

13 G. M. Sheldrick, *Acta Crystallogr., Sect. A*, 1990, **46**, 467.

14 G. M. Sheldrick, *SHELXL-93, a Program for the Refinement of Crystal Structure Determination*, University of Göttingen, 1993.

15 D. Massiot, B. Touzo, D. Trumeau, J. P. Coutures, J. Virlet, P. Florian and P. J. Grandinetti, *Solid State NMR,* 1996, **6**, 73.

16 M. Smith, *Appl. Magn. Reson.*, 1993, **4**, 1.

17 L. Frydman and J. S. Harwood, *J. Am. Chem. Soc.*, 1995, **117**, 5367.

18 A. Medek, J. S. Harwood and L. Frydman, *J. Am. Chem. Soc.*, 1995, **117**, 12779.

19 Ch. Fernandez and J. P. Amoureux, *Chem. Phys. Lett.*, 1995, **242**, 449.

20 Ch. Fernandez and J. P. Amoureux, *Solid State NMR*, 1995, **5**, 315.

21 P. J. Grandinetti, RMN program, available at the Department of Chemistry, Ohio State University, 1991.

22 D. Massiot, H. Thiele and A. Germanus, *Bruker Rep.*, 1994, **140**, 1762.

23 P. A. Stadelman, *Ultramicroscopy*, 1987, **21**, 131.

24 P. E. Werner, L. Eriksson and J. Westdahl, *J. Appl. Crystallogr.*, 1985, **18**, 367.

25 G. Yamaguchi, M. Okumiya and S. Ono, *Bull. Chem. Soc. Jpn.*, 1969, **42**, 2247.

26 M. Okumiya and G. Yamaguchi, *Bull. Chem. Soc. Jpn.*, 1971, **44**, 1567.

27 N. E. Breese and M. O'Keeffe, *Acta Crystallogr., Sect. B*, 1991, **47**, 192.

Paper 7/00054*E*; *Received* 2nd *January*, 1997